Fiber and Integrated Optics

ISSN: (Print) (Online) Journal homepage: https://www.tandfonline.com/loi/ufio20

High-Sensitive Acoustic Sensor Based on Microfiber Mach–Zehnder Interferometer with Tapered Polarization-Maintaining Fiber

Xiaojun Zhu, Wen Liu, Dan Sun, Guoan Zhang, Li Zou, Zhipeng Liang, Zhanghua Han & Yuechun Shi

FIBER AND INTEGRATED OPTICS
https://doi.org/10.1080/01468030.2022.2042626

High-Sensitive Acoustic Sensor Based on Microfiber Mach–Zehnder Interferometer with Tapered Polarization-Maintaining Fiber

Xiaojun Zhu [a], Wen Liu [a], Dan Sun [a], Guoan Zhang [a], Li Zou [a], Zhipeng Liang [a], Zhanghua Han [b], and Yuechun Shi [c]

[a]School of Information Science and Technology, Nantong University, Nantong, Jiangsu province, China; [b]Shandong Provincial Key Laboratory of Optics and Photonic Devices and Shandong Provincial Engineering and Technical Center of Light Manipulations, School of Physics and Electronics Shandong Normal University, Jinan, Shandong province, China; [c]Key Lab Intelligent Opt Sensing & Manipulat, Minist Educ, Nanjing University, Nanjing, Jiangsu province, China

ABSTRACT

We propose a high sensitive acoustic sensor based on a microfiber Mach-Zehnder interferometer (MMZI) with tapered polarization-maintaining fiber (PMF). The optical tapering technology is used to taper the PMF. Then, the MMZI is attached to a wood pulp diaphragm (WPD) to form an acoustic sensor, whose curvature will change with the vibration of the diaphragm. Two sensors with different waist diameters are made for performance comparison. Experimental results show that the acoustic sensor can achieve a wideband frequency response range from 200 Hz to 4000 Hz. The responses are flat at frequencies ranging from 200 Hz to 1500 Hz. Moreover, we find that the sensing performance of the acoustic sensor improves with the decrease in its waist diameter. When the waist diameter is 25.72 μm, the response sensitivity of the sensor can reach 42.4 mV/kPa at 2000 Hz, and the minimum detection pressure is 1.24 Pa/√Hz. It provides an effective way to fabricate an acoustic sensor, with low cost, easy integration, and high sensitivity.

ARTICLE HISTORY
Received 15 November 2021
Accepted 11 February 2022

KEYWORDS
Acoustic sensor; Mach-Zehnder interferometer; polarization-maintaining fiber; tapered fiber

1 Introduction

Acoustic sensors have been significantly developed in response to the needs of oil exploration, national defense, medical treatment, mobile communications, bioacoustics, and seismic monitoring [1–6]. At present, acoustic sensing mainly depends on electromagnetic sensing. Traditional electromagnetic sensing is easily affected by external electromagnetic interference. Compared with them, optical fiber sensor has been developed rapidly due to its good stability of resistance to electromagnetic radiation, small size, lightweight, high multiplexing ability [7–11]. In 1977, Bucaro et al. first proposed an acoustic sensor by adopting a dual-optical path interferometer system based on single-mode (SMF) and multimode fiber (MMF) [12]. After that, several acoustic sensors

CONTACT Xiaojun Zhu zhuxj0122@ntu.edu.cn School of Information Science and Technology, Nantong University, Nantong 226019 China

based on different structures and types of optical fiber are reported [13–21]. Among them, acoustic sensors based on optical fiber interferometers have attracted more attention due to their simple structure and compact sizes, such as Fabry–Pérot interferometer (FPI), Michelson interferometer, Sagnac interferometer, and Mach–Zehnder interferometer (MZI) [22–26]. In general, it is difficult for Sagnac sensors to simplify the sensor structure while enhancing the performance. FPI does not have the ability of temperature self-compensation. Comparatively, MZI shows great application prospects in acoustic sensing with the advantages of high sensitivity, fast response, and good performance. In 2018, Lan et al. proposed a three-dimensional shaped Mach–Zehnder optical fiber sensor that can detect ultrasonic signals in a specific frequency response range [25]. However, the sensitivity depends on the sensing length, which needs to be achieved by using relatively limited space and a long optical fiber (up to several meters long). In 2020, Zhu et al. proposed a membrane-free acoustic sensing method based on the Mach-Zehnder interferometer [26]. The sensing principle depends on the direct detection of the refractive index change caused by the acoustic pressure in the open cavity. Due to the limitation by the fiber core, high-order modes were difficult to be excited from the fundamental mode, which restricted the improvement of the sensitivity.

In recent years, micro-fiber MZI (MMZI) has attracted wide attention because of its low coupling loss, and high evanescent field. In 2018, Sumit et al. proposed a compact diaphragm-free optical microphone consisting of a tapered micro-tip in a cantilever configuration for detecting low-frequency acoustic signals [27]. The maximum acoustical sensitivity was 10.63 mV/Pa, and the linear frequency range was 0–400 Hz. Due to the bulky structure of the optical cantilever, the sensor was hard to adjust the distance between the optical fiber tip and the single-mode fiber (SMF). It prevents sensitivity enhancement and limits the low-frequency response. In the same year, Zhao et al. proposed an in-line fiber low-frequency acoustic sensor based on Butterfly-Shape MZI, in which a tapered hollow-core fiber (HCF) is sandwiched between two single-mode fibers (SMFs) [28, 29]. However, the low resonant frequency of the vibration platform limits the improvement of the sensitivity. Moreover, the photoelectric demodulation in free space leads to the non-integration of the system and the increase in production cost.

In this paper, we propose a highly sensitive acoustic sensor. The polarization-maintaining fiber (PMF) is tapered to form the MMZI as the sensing head. The MMZI with a waist diameter of 25.72 μm is attached to the center of the WPD for acoustic detection. A fiber Bragg grating (FBG) is combined to develop an all-fiber demodulation device for demodulating the optical signals. The acoustic sensor can achieve a broadband frequency response for acoustic signals ranging from 200 Hz to 4000 Hz, where the sensor has a flat response in the range of 200 Hz to 1500 Hz. When the vibration frequency of the WPD is

2000 Hz, the maximum of the acoustical sensitivity is about 42.4 mV/kPa. Moreover, two sensors with different waist diameters are fabricated to detect the acoustic signals. The measurement results indicate that the smaller the waist diameter of the optical fiber is, the better performance the sensor will perform. This kind of all-fiber demodulated micro-optical fiber acoustic sensor probably has a broad application prospects in the field of optical fiber sensing and provides a feasible solution for the preparation of highly sensitive and highly integrated acoustic sensors.

2 Sensing design and theoretical analysis

2.1 Sensing design

The MMZI is fabricated using optical taper technology, and the experimental setup is shown in Figure 1. We use Panda-type PMF (THORLABS, PM1550-XP) for the experiments, in which the diameters of the core, the stress zone, and the cladding are 8 μm, 20 μm, and 125 μm, respectively. A segment of PMF is fused between two SMFs, and then both sides of the PMF are fixed on the optical fiber holders. By accurately controlling the flame temperature and the position of the translation stations, a tapered PMF can be obtained by designing the control software of the hydrogen-oxygen flame tapering machine. The moving speeds of the flame sweeping and the translation station are 2.5 mm/s and 0.08 mm/s, respectively. In the whole tapering process, one of the SMF is connected to an amplified spontaneous emission (ASE, Opeak LSM-ASE-C-F) and the other is connected to an optical spectrum analyzer (OSA, Yokogawa AQ6370B) for real-time detection of the spectrum of the MMZI.

Figure 2 shows the schematic diagrams and microscope image of each section of the MMZI. The total length of the tapered fiber L is 2 cm, and the waist diameter of the tapered fiber is 25.72 μm. In the initial stage of the tapering, the two internal stress rods of the PMF are kept valid, which maintains good refractive index distribution and polarization characteristics. In the

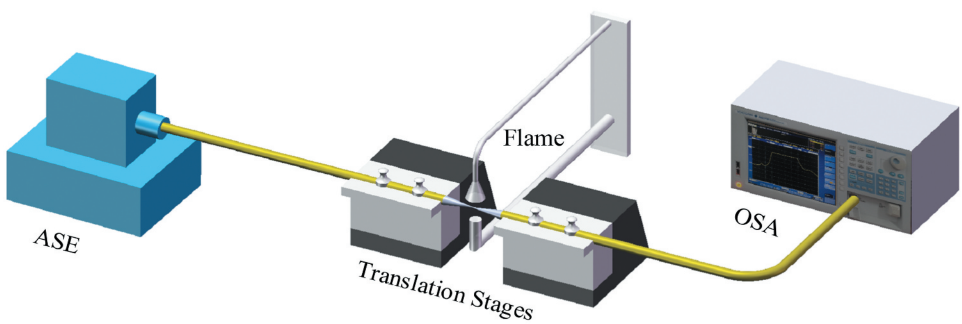

Figure 1. Schematic diagram of experimental setup for fabricating the MMZI by a hydrogen-oxygen taper machine.

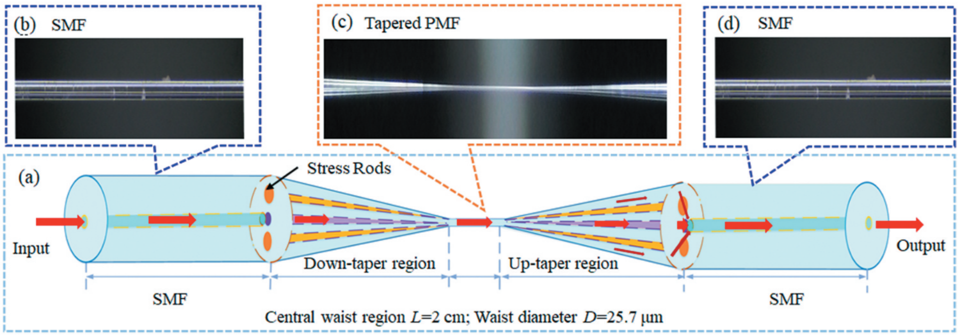

Figure 2. (a) Schematic diagram and optical field distribution of the MMZI. (b) the microscope image of the left SMF. (c) the microscope image of the tapered PMF. (d) the microscope image of the right SMF.

process of tapering, the stress rods in the center of PMF are destroyed at high temperature, thus forming a polarization-maintaining-non-polarization-maintaining structure. Light is injected into the core of the PMF. In the tapered region of the PMF, the diameter of the PMF decreases gradually. When the diameter is less than the diameter of the mode field, the light leaks from the core to the cladding of the PMF, resulting in two path transmission in the MMZI. Due to the direct fusion between the tapered PMF and the SMF, the higher-order cladding mode and the fundamental core mode light can couple to the core of the SMF. Therefore, the interference occurs when the light returns to the SMF. Figure 3 shows the transmission spectrum of the MMZI with different waist diameters. Figure 3(a) shows the transmission spectrum of the MMZI with waist diameters of 28.4 μm. Four channels are formed in the wavelength range from 1525 nm to 1570 nm. The extinction

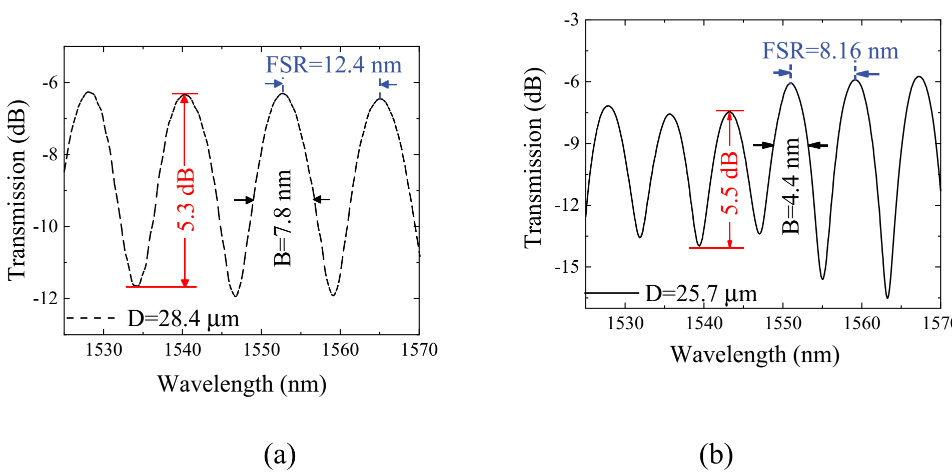

Figure 3. The transmission spectrum of MMZI with different waist diameters. (a) the waist diameter is 28.4 μm. (b) the waist diameter is 25.7 μm.

ratio (ER) is 5.3 dB, and the free spectral range (FSR) is 12.4 nm. Figure 3(b) shows the transmission spectrum of MMZI with a waist diameter of 25.7 μm, in which six channels are formed, the ER is 5.5 dB, and the FSR is 8.16 nm. From Figure 3, we can see that the MMZI has a good filtering function, in which the features of the transmission spectrum can be designed by changing the tapered fiber. The transmission spectrum of MMZI will be shifted by changing the curvature of the MMZI. By monitoring the transmission spectrum of the MMZI, the curvature can be measured in real-time. Accordingly, the external acoustic frequency can be obtained by measuring the vibration frequency of the MMZI when the acoustic pressure transmits on the fiber.

The MMZI is connected to the WPD as the sensor head, which is shown in Figure 4. A vibrating film is fabricated by a 55 mm thickness polyethylene sheet with a through-hole of radius of 125 mm drilled on it. The WPD with a thickness of 0.413 mm is attached to the polyethylene sheet with polymer-based adhesive. The WPD acts as a diaphragm with a round hole. Then, the MMZI is attached to the central position of the WPD. Figure 5(a) is an experimental configuration for an acoustic sensor system based on WPD. Figure 5(b) is the system block diagram. The acoustic sensors consisting of the MMZI and the WPD are placed on the far side of the vibration-free worktable. The light from the ASE is input into the acoustic sensor from port 1 of an optic fiber circulator (OFC). The light transmits from port 2 of the OFC and is reflected by the FBG, and then enters port 3 of the OFC when the light satisfies the Bragg condition. The central wavelength of the FBG is 1550.26 nm. The light output from Port 3 of the OFC will be converted into an electrical signal by a photodetector (PD, Thorlabs DET08CFC/M) and then measured by a digital storage oscilloscope (DSO, Agilent DSO90604A). A reference acoustic signal is generated by an audio signal generator (ASG) from a computer, which can also be monitored by the DSO. The reference signal and the output signal from the sensor are shown on DSO for comparison and analysis. Thus, we can obtain the sensing characteristics of the acoustic sensor. It should be illustrated that to promote the performance of the demodulation of the vibration, a region of a linear transmission spectrum of the MMZI is chosen as the demodulation waveband of FBG, as shown in Figure 3 Figure 4 and (the inset figure). The reflection wavelength of FBG will always be located in this region. When the WPD vibrates, the transmission spectrum of the MMZI will shift. The amplitude of the reflected light from FBG will have a better linear response to the vibrating. Therefore, when the acoustic signal is sinusoidal, the signal output from the PD is also sinusoidal due to the better demodulator composed of the FBG and the MMZI.

When the ASG inputs a signal to the acoustic sensor, it induces the vibration of the WDP. The wavelength spectra of the MMZI shifts, and the amplitude of the light reflected by the FBG changes. Therefore, the acoustic

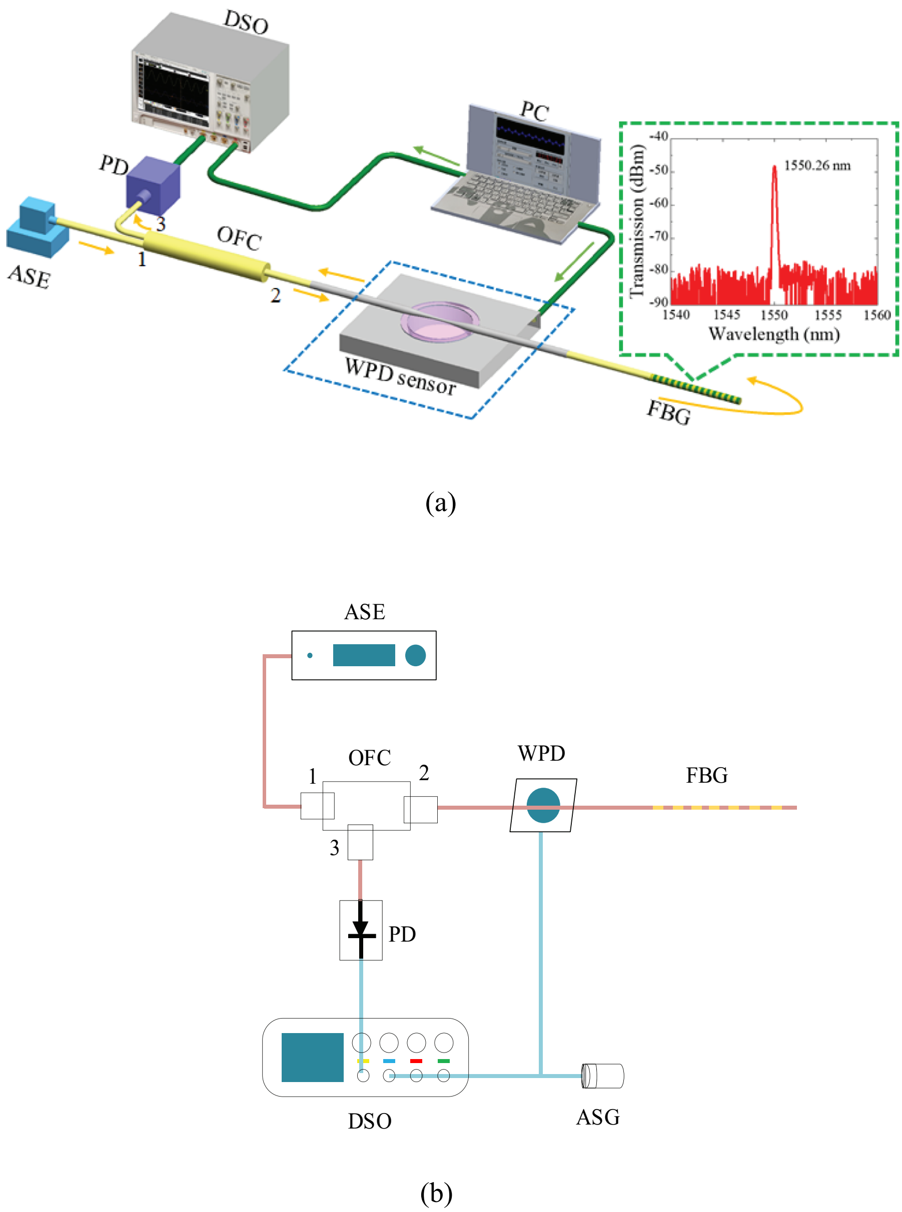

Figure 4. Schematic diagram of the acoustic sensor composed of MMZI and WPD. Figure 5.(a) Schematic diagram of the experimental setup of the acoustic sensor system. inset: the reflection spectrum of FBG. (Yellow line: the transmission of optical signal; Green line: the transmission of the electrical signal). (b) System block diagram.

sensor can detect the frequency and amplitude of the acoustic signal. In our experiment, the two interfaces of the DSO represent the signals from the detection of the acoustic sensor and the reference acoustic signal, respectively.

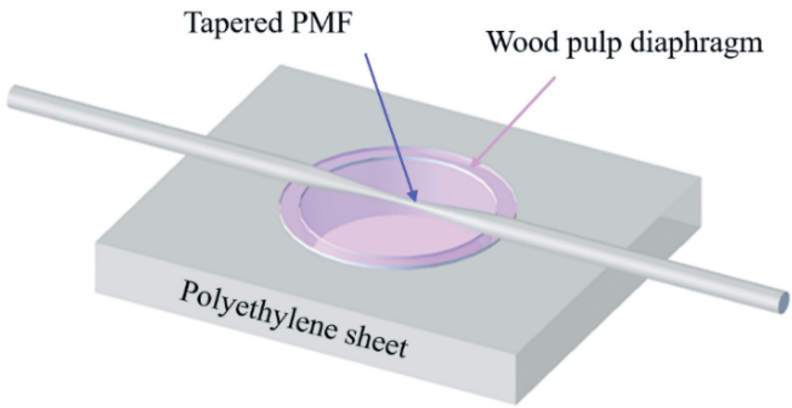

Figure 5. (a) Schematic diagram of the experimental setup of the acoustic sensor system. inset: the reflection spectrum of FBG. (Yellow line: the transmission of optical signal; Green line: the transmission of the electrical signal). (b) System block diagram. Figure 4.Schematic diagram of the acoustic sensor composed of MMZI and WPD.

2.2 Theoretical models

The phase expression is

$$\varphi = \frac{2\pi n L_1}{\lambda_c} \tag{1}$$

where n represents the refractive index of the light, L_1 represents the length of the light, and λ_c represents the central wavelength of the light. The initial phase expressions of the corresponding optical fiber cladding mode and core mode are as follows

$$\varphi_{clad} = \frac{2\pi n_e^{clad,m} L_2}{\lambda_c} \tag{2}$$

$$\varphi_{core} = \frac{2\pi n_e^{core} L_2}{\lambda_c} \tag{3}$$

From the Eq. (2) and (3), the expression of the phase difference between the cladding mode and the core mode can be obtained as follows

$$\Delta\varphi = \varphi_{core} - \varphi_{clad} = \frac{2\pi}{\lambda_c}\left(n_e^{core} - n_e^{clad,m}\right)L_2 = \frac{2\pi \Delta n_e L_2}{\lambda_c} \tag{4}$$

where $n_e^{clad,m}$ is the effective refractive index (ERI) of the m-order cladding mode, n_e^{core} is the ERI of the core mode, Δn_e is the difference between the ERI of the cladding mode and the core mode, and L_2 is the interference length of MMZI.

When the phase is equal to 2 $m\pi$, the light intensity of the optical fiber interference spectrum will reach the maximum, and when the phase is equal to (2 m+ 1) π, the light intensity of the optical fiber interference spectrum will reach the minimum value (m is a positive integer).

The wavelength of the peak of the interference spectrum can be expressed as follows:

$$\lambda_{\mathrm{p}} = 1\Delta n_{\mathrm{e}} L_2 \tag{5}$$

The wavelength of the trough of the interference spectrum can be expressed as:

$$\lambda_d = \frac{2}{2m+1} \Delta n_e L_2 \tag{6}$$

The FSR of the interference spectrum is expressed as follows:

$$\Delta\lambda = \frac{\lambda^2}{\Delta n_e L_2} \tag{7}$$

Interference spectrum ER is an important parameter to describe optical interference, which can be defined as:

$$ER = \frac{I_{\max} - I_{\min}}{I_{\max} + I_{\min}} = \frac{2\sqrt{I_{\mathrm{core}} I_{\mathrm{clad}}}}{I_{\mathrm{clad}} + I_{\mathrm{core}}} \tag{8}$$

In the process of tapering, as the waist diameter of the fiber becomes small, the light intensity of the cladding mode increases, and the comb spectral density increases. When the wavelength is constant, the effective propagation constant of the fundamental mode will also become smaller. More optical power is distributed in the cladding, which increases the loss.

When the curvature of the MMZI changes under the influence of acoustic pressure, the transmission spectrum will shift. This allows it to be used as an acoustic pressure sensor for acoustic frequency detection.

When the fiber is bent, different strains occur in the core and cladding, resulting in a change in the difference of the ERI between the core mode and the cladding mode. The difference of the ERI can be expressed as:

$$\Delta n_{eff} = \Delta n_{eff}^{0} + k\Delta\varepsilon \tag{9}$$

where, Δn_{eff}^{0} is the difference of ERI when the fiber strain is free, and k is the refractive index coefficient (RIC) of the strain. The strain difference between the cladding and the core is

$$\Delta\varepsilon = \frac{d}{R} \tag{10}$$

where d is the distance between the cladding and the core, and R is the curvature radius. The intensity of transmission reaches its valley value at the wavelength as follow

$$\lambda_m = \frac{2\Delta n_{eff}\ L}{2m+1} \tag{11}$$

By substituting Eq. (2) and (3) into (4), the valley wavelength of interference fringes can be obtained as

$$\lambda_m = \frac{2\Delta n^0_{eff}\ L}{2m+1} + \frac{2kLd}{2m+1} \cdot \frac{1}{R} \tag{12}$$

It can be seen from Eq. (5) that due to the value of k being negative, the interference wavelength is blue-shifted with the increase in curvature ($1/R$).

The curvature experimental setup is shown in Figure 6. Fix the MMZI to the fiber clamp, and then place the clamper on the curvature measuring platform. The curvature of MMZI can be adjusted by changing the position of the displacement platform perpendicular to the two cylindrical axes. The displacement platform is placed in the center of the MMZI, and keeping the interval l_0 between the two cylindrical axes fixed, and the offset displacement is represented by x. Then, the curvature of the MMZI varies with the movement of the mobile station (the arrow is the moving direction). Then, the curvature C of the MMZI can be expressed as

$$\frac{1}{C} = R = \frac{x}{2} + \frac{l_0^2}{8x} \tag{13}$$

where R is the radius of curvature. In this experiment, l_0 is 0.175 m.

By choosing the dip wavelength of 1 548.74 nm as the detection wavelength, the transmission spectra vary with the changing of curvatures, as shown in Figure 7. We can see that with the curvature increasing, the transmission spectra of the MMI are blueshifted. There is also a well linear response relationship between wavelength and curvature, as shown below:

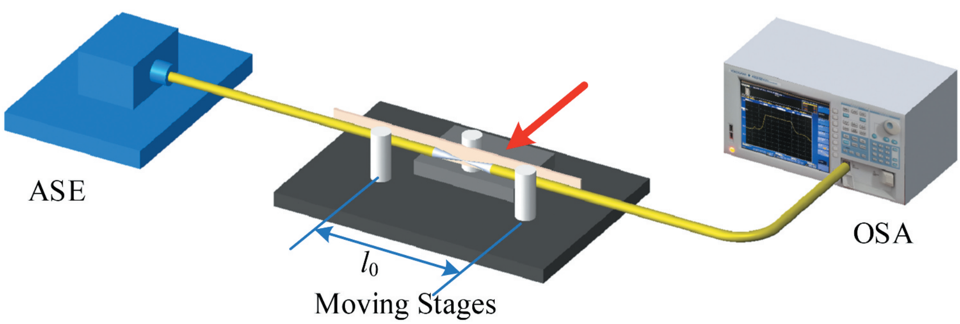

Figure 6. Diagram of experimental equipment for curvature measurement.

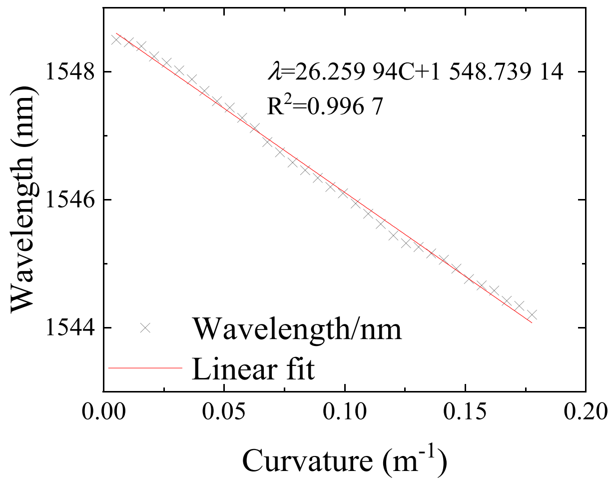

Figure 7. Experiment and fitting curve of wavelength and curvature.

$$\lambda = -26.25994C + 1548.73914 \tag{14}$$

We chose wood pulp material to make vibration diaphragm because the wood pulp material has a low elastic modulus (3.78×10^9 Pa), a well steady-state vibration, and transient vibration characteristics [30]. The curvature of the sensor mainly depends on the design of the diaphragm, and the conventional method to study the elastic properties of the diaphragm is the load-deflection method [31]. In the experiment, a circular diaphragm is chosen as the diaphragm format, in which there is no non-linear term in the load–deflection relationship. The change of the MMZI curvature caused by the central deformation of the diaphragm is defined as [32]:

$$\Delta d = \frac{3(1-\mu^2)r^4P}{16t^3E}\frac{f_m^2}{\sqrt{(f_m^2-f^2)^2+4f^2\xi^2}} \tag{15}$$

where, μ and E are the Poisson's ratio and Young's modulus of the diaphragm material, r is the diaphragm radius, P is the external acoustic pressure, t is the diaphragm thickness, f is the acoustic frequency, ξ is the damping coefficient, and f_m is the m-order intrinsic frequency of the diaphragm, respectively.

To obtain high acoustic sensitivity, we need to increase the external acoustic pressure on the diaphragm to generate large deformations on the MMZI. By increasing the ratio of diameter to thickness, as described in Eq. (15), the diaphragm deformation can be increased for a given diaphragm material, and the acoustic sensitivity of the sensor can be improved. The first-order natural frequency (f_0) will decrease as shown in [32]:

$$f_0 = \frac{10.17t}{r^2}\sqrt{\frac{E}{12\rho(1-\mu^2)}} \tag{16}$$

From Eq. (16), we can obtain the change of the first-order natural frequency of the WPD with different radius and thicknesses as shown in Figure 8. The calculation parameters are as follows: Poisson's ratio (μ) = −0.7, Young's modulus € = 3.78 GPa, and material density (ρ) = 2188 kg/m^3. From Figure 8, we can see that the first-order natural frequency of the WPD is 2479 Hz when the radius is 30 mm and the thickness is 413 µm.

We also calculate the central deformation of the diaphragm when the applied acoustic pressure is 1 Pa. We analyze the effect of acoustic pressure on the structure of the wood pulp diaphragm. When acoustic frequencies change from 0 Hz to 5000 Hz, the deformations of the diaphragm are shown in Figure 9. In the frequency range of 0 – z – 1500 Hz, the central deformations of the diaphragm change from 0.29 µm to 0.46 µm, which shows that the curvature offset is almost unchanged. When the acoustic frequency is greater than 1500 Hz, the offset begins to increase exponentially. The maximum offset is generated at its resonance frequency (2479 Hz) with a value of 2.4 mm. Finally, by continually increasing the frequency, the deformations begin to decrease from 17.09 µm to 0.09 µm (around 5000 Hz).

The MMZI can detect the acoustic signal due to its transmission spectrum shifting with the curvature change. When there is no external acoustic signal, the curvature of MMZI is constant, and the transmission spectrum does not change. The PD outputs a stable DC signal, which is shown on the DSO screen.

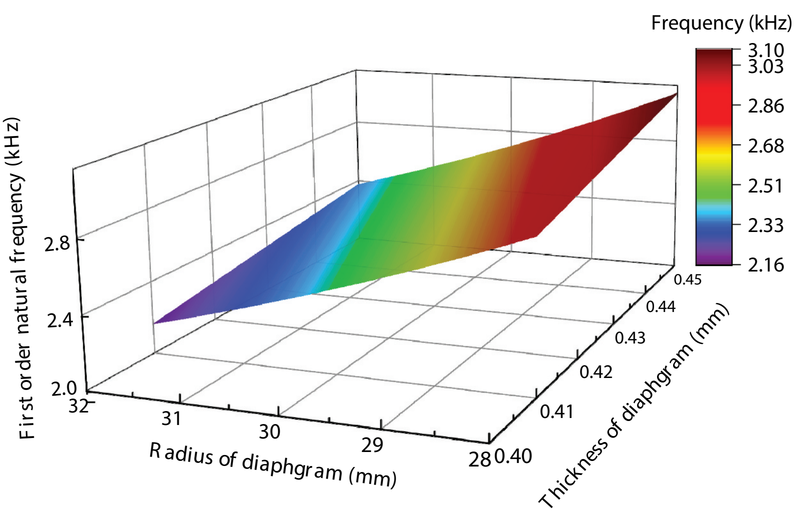

Figure 8. First-order natural frequency of WPD versus radius and thickness.

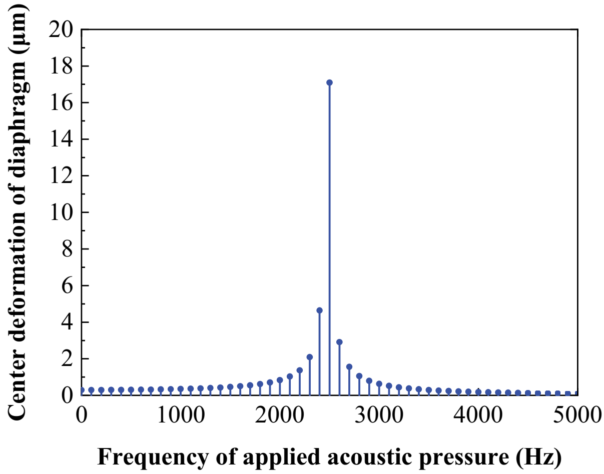

Figure 9. The center deformation offset of the diaphragm relative to the initial position versus frequency under the action of 1 Pa acoustic pressure.

Under the acoustic pressure, the intensity of the reflected light from FBG will change accordingly with the vibration of the WPD. The vibration signal from WPD satisfies:

$$E = A\sin(2\pi ft) \tag{17}$$

where A is the amplitude of vibration and f is the acoustic frequency.

When the acoustic signal acts on the MMZI through the diaphragm, the MMZI is subjected to radial stress because the sound is a longitudinal wave. Taking the diameter of the optical fiber D into consideration, the radial stress causes the curvature change and the phase change of the MMZI is expressed by:

$$\Delta\varphi = k_0 n L_2 \left[\frac{D}{k_0 n}\frac{\partial\beta}{\partial D} - \frac{1}{2}n^2(P_{11} + P_{12})\right]\varepsilon_1 \tag{18}$$

where k_0 is the wavenumber of light in vacuum, $\partial\beta\,/\partial D$ is the change of propagation constant, P_{11} and P_{12} are the photoelastic coefficients of the optical fiber, and ε_1 is the transverse strain of the optical fiber.

When there is stress, replace $\Delta\lambda$ into the Eq. (18), the offset of the peak value of the transmission spectrum of the MMZI is obtained by:

$$\Delta\lambda = \frac{\lambda_c^2}{\Delta n_e L_2}\frac{\Delta\varphi}{2\pi} \tag{19}$$

The micro-deformation of the MMZI should satisfy the same vibration function as the acoustic signal. When the acoustic signal is the sinusoidal format, the phase change of MMZI can be expressed as:

$$\Delta\varphi = k_0 n L_2 \left[\frac{D}{k_0 n}\frac{\partial\beta}{\partial D} - \frac{1}{2}n^2(P_{11} + P_{12})\right]\varepsilon_1 \sin(2\pi f t) \tag{20}$$

If the Bragg reflection peak wavelength of FBG is λ_F, then the light intensity of MMZI at wavelength λ_F is:

$$\begin{aligned} I_M = {} & I_1 + I_2 \\ & + 2\sqrt{I_1 I_2}\cos\left\{\frac{2\pi}{\lambda_F} n L_M \left[\varepsilon_3 - \frac{1}{2}n^2(P_{11} + P_{12})\varepsilon_1 - \frac{1}{2}n^2 P_{12}\varepsilon_3\right]\sin(2\pi f t)\right\} \end{aligned} \tag{21}$$

The reflectivity of FBG is:

$$R = \frac{kk^* \sinh^2(\gamma L_F)}{\gamma^2 \cosh^2(\gamma L_F) + \delta^2 \sinh^2(\gamma L_F)} \tag{22}$$

where I_1 is the fundamental mode light field, I_2 is the mode light intensity in the cladding, L_M is the length of the light passing through the PMF, ε_3 is the longitudinal strain of the fiber, and δ represents the initial phase of the light.

Then, the light intensity detected by the photodetector is:

$$I_p = I_M R \tag{23}$$

From Eq. (23), we can see that the sensitivity of the signal can be improved by changing the parameters of the fiber, such as increasing the transverse strain ε_1 by reducing the diameter of the fiber. Therefore, it is easier for our acoustic sensor systems to detect the high frequency and weak signals due to the curvature sensitivity of the MMZI.

3 Experimental results and analysis

By fixing the output power of the ASG at 25 W, we use the acoustic sensor for detecting the sinusoidal signals generated from ASG with different frequencies, as shown in Figure 10. In Figure 10, the "Input" represents the reference signal. The "Output" is the detected signal from the acoustic sensor. From Figure 10(a), we can see that the initial frequency of the standard sinusoidal signal generated from ASG is 200 Hz. The detected signal generated from the acoustic sensor is also a standard sinusoidal signal consistent with the ASG, as shown in Figure 10a(ii). Figure 10a(iii) is the frequency after Fourier transforms from the detecting signal. We can see that the frequency distribution after Fourier transform is a singularity. The peak frequency is 200 Hz that is corresponding to the frequency of the ASG. When the frequency increases from 200 Hz to 4000 Hz, the acoustic sensor also responds well to the signals generated by ASG, as shown in Figure 10(b-d). Comparing the inputs and outputs, we find that the detected signals are consistent with the reference

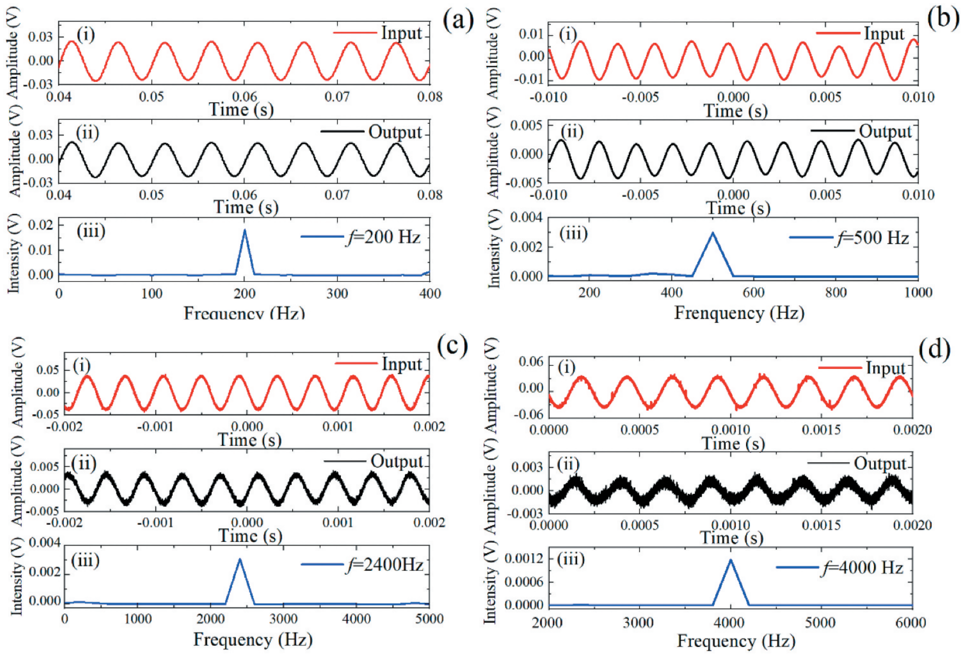

Figure 10. Comparison of the signals detecting from the acoustic sensor and the ASG with different frequencies. (a) f = 200 Hz. (b) f = 500 Hz. (c) f = 2 400 Hz. (d) f = 4 000 Hz. (i) represent the detected signals from the ASG. (ii) express the signals detected by the acoustic sensors based on the MMZI. (iii) are the Fourier transform of the signal detected from the acoustic sensor in the frequency domain.

signals, which shows that the acoustic detection system fabricated by the MMZI has a good capability of signal demodulation and audio vibration response.

In our experiment, we have fabricated two acoustic sensors with different waist diameters of tapered PMF: Sensor-1 and Sensor-2. The original length of PMFs are 20 mm; then, Sensor-1 is tapered 10.493 mm with waist diameter 25.72 µm, and Sensor-2 is tapered 9.458 mm with waist diameter 28.39 µm. Figure 11 shows the output signals of the two sensors recorded by the DSO when a reference acoustic signal is 1000 Hz and an acoustic signal of 71 Pa. The corresponding frequency responses are recorded by Fourier transform as shown in Figure 12. It can be observed that the noise floor of Sensor-1 and Sensor-2 at 1000 Hz are about −88.62 dB and −85.41 dB, respectively. Under an external acoustic pressure of 71 Pa, the signal-to-noise ratios (SNRs) of Sensor-1 and Sensor-2 are 58.32 dB and 46.2 dB, respectively.

Taking Sensor-1 as an example, we study the performance of the proposed sensors under different acoustic pressures. Two signals with different intensities act on Sensor-1 to measure the responses with the same frequency of 2000 Hz as shown in Figure 13. When the external acoustic pressures increase

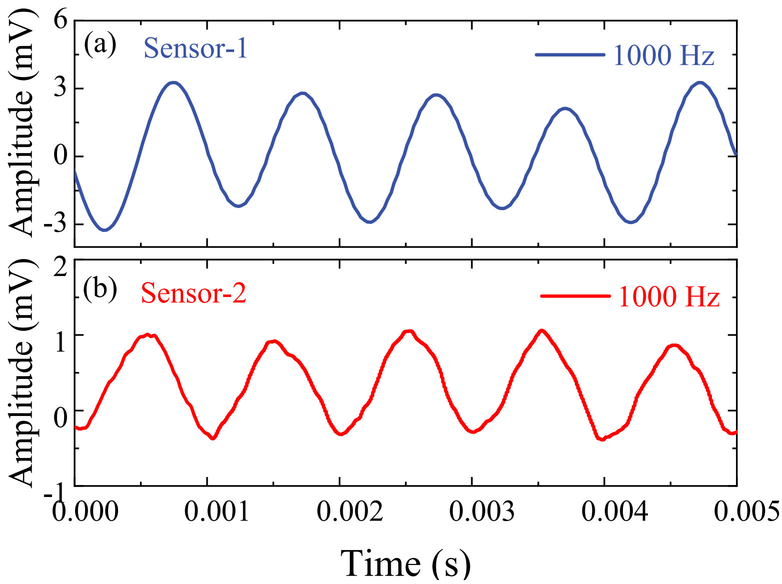

Figure 11. Time domain response to the external acoustic signal at 1000 Hz of Sensor-1 and Sensor-2. (a) Sensor-1. (b) Sensor-2.

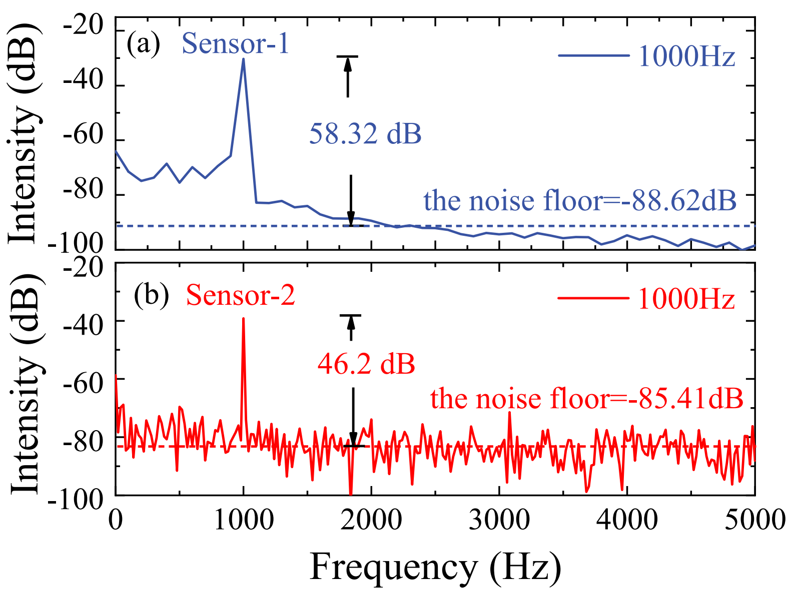

Figure 12. Frequency domain response to the external acoustic signal at 1000 Hz of Sensor-1 and Sensor-2. (a) Sensor-1. (b) Sensor-2.

from 42 Pa to 96 Pa, the amplitude of Sensor-1 increases from 1.8 to 4.2. The amplitude response of the sensor is proportional to the intensity of the external acoustic pressure.

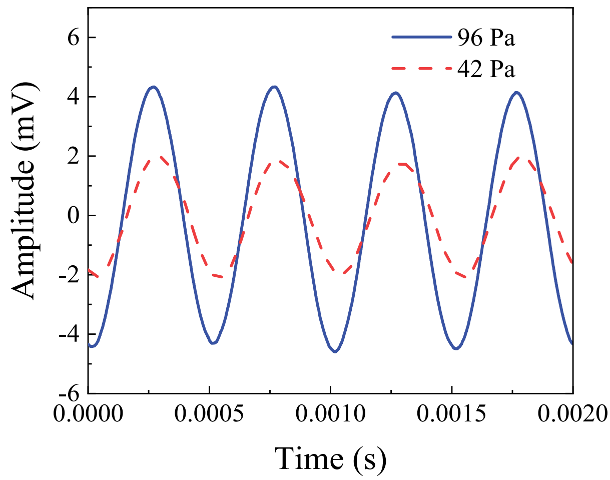

Figure 13. Time domain response of Sensor-1 to acoustic signals with different intensities of 2000 Hz.

We also test the relationship between the acoustic sensitivity and the frequency response of Sensor 1 and Sensor 2 as shown in Figure 14. From Figure 14, we can see that both frequency responses of the sensors are relatively uniform and flat in the range from 200 Hz to 1500 Hz. The sensitivities of both sensors begin to quickly increase after 1500 Hz and reach a maximum at a frequency of 2500 Hz, in which the frequency of the maximum sensitivity is equivalent to the first-order natural frequency of WPD. This is to say that there is a linear relationship between the output signal and the applied acoustic pressure. By repeating similar experiments on the sensors, the results comply

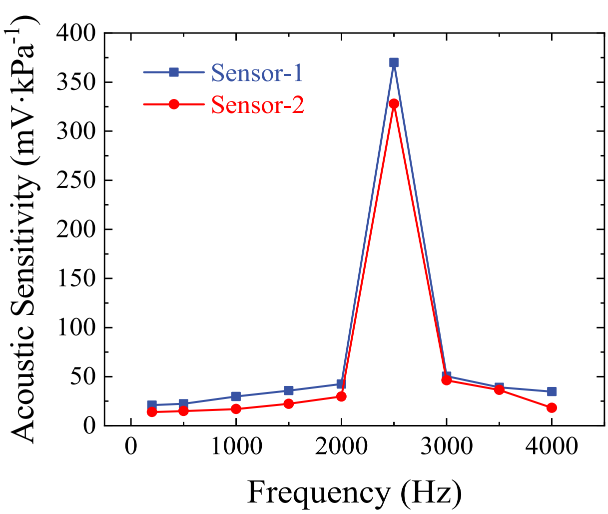

Figure 14. Relationship between the acoustic sensitivities and frequency responses of the sensors.

with the linear relationship and are also consistent with the theory of Eq. (16). When the acoustic signal is 2000 Hz, the acoustic sensitivities of Sensor-1 and Sensor-2 are 42.4 mV/kPa and 29.8 mV/kPa by calculating.

In order to study the features of the sensor under different acoustic pressures, we measure the sensitivities of the MMZI with various intensities in 2500 Hz acoustic signals. The time domain responses of sensor-1 are shown in Figure 15(a). With the increase in the external acoustic pressure, the vibration amplitude of the response signal also increases. The relationship between the output voltage and the applied acoustic pressure is shown in Figure 15(b). The sensitivity of sensor-1 determined by the slope of the linear fitting curve at 2500 Hz is 370 mV/kPa.

To analyze the noise level of both sensors, the noise signals of the PD without any external acoustic signal are shown in Figure 16. The noise signals of Sensor-1 and Sensor-2 are 0.053 mV and 0.037 mV, respectively. After the calculation, the minimum detection pressure of Sensor-1 and Sensor-2 is 1.24 Pa/√Hz and 1.26 Pa/√Hz, respectively. It should be emphasized that the enhanced performance of this acoustic sensor can be used as a hydrophone in the detection at lower frequencies.

In order to highlight the advantages of our sensors, the performance of several types of other sensors and our designed ones are shown in Table 1. The sensor of the cantilever structure is bulky and hard to integrate [27, 33]. The diaphragm sensor has the drawback of complex fabrication and demodulation without an all-fiber format [34]. The other sensors reported are insufficient either in the dynamic response range or in sensitivity [15, 28, 35]. Therefore, our proposed acoustic sensor based on the MMZI that we proposed has the advantages of simple structure, convenient demodulation, high sensitivity, and a broad response range.

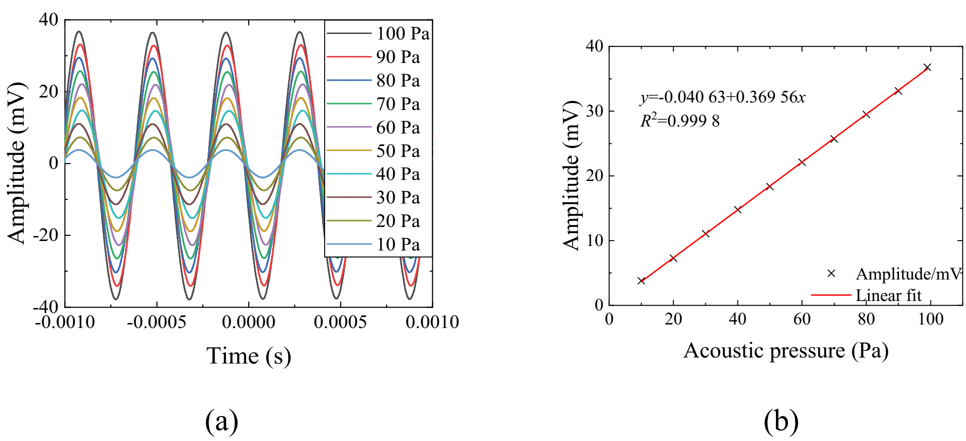

Figure 15. Acoustic pressure sensitivity at 2500 Hz. (a) The time domain response of sensor-1 to the external sound signal with a frequency of 2500 Hz and different acoustic pressure. (b) Response and linear fitting of sensor-1 to different acoustic pressure.

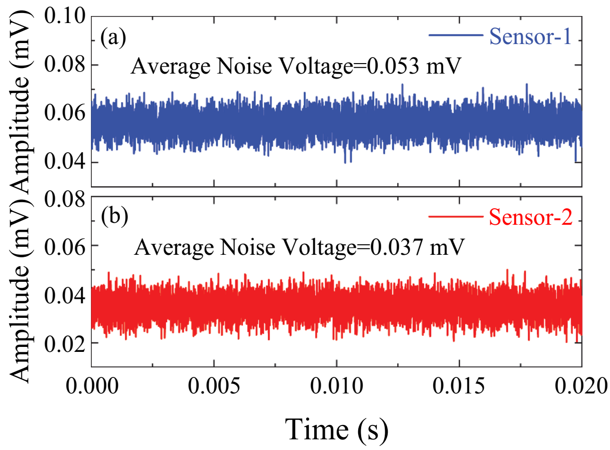

Figure 16. Noise signal of both sensors without any external acoustic signal. (a) Sensor-1. (b) Sensor-2.

Table 1. Comparison of optical fiber acoustic sensors.

Acoustic sensor	Structure	Response range	Sensitivity	Practicability
Diaphragm-free optical microphone [27]	Cantilever tapered tip	0 Hz-400 Hz	10.63 mV/Pa	The structure of cantilever beam is bulky, and the response at low frequency is limited.
Butterfly-Shape MZI [28]	Fusion of tapered hollow fiber between two single-mode fibers	0.1 w-0.5 w	13.5 dB/w	The demodulation is complex and the cost is high.
Fiber optic Fabry-Perot acoustic sensor [33]	Flexible FP cavity made of polydimethylsiloxane and compact optical fiber cantilever beam with low moment of inertia	Up to 20 kHz	0.088 mV/mPa	The structure is complex and has high requirements for the process.
Nitrile diaphragm acoustic sensor [34]	Tapered optical fiber structure attached to nitrile-butadiene polymer base film	200 Hz-5000 Hz	36 mV/kPa	Low sensitivity
All-optical fiber acoustic sensor [35]	Single mode-few mode-single mode offset splicing	110 Hz-230 Hz	4.5 mV/Pa	Small measuring range
Hollow core optical fiber acoustic sensor [15]	Two tapered plugs are connected in the hollow optical fiber segment by welding.	200 Hz-1200 Hz	Sensitive response	It requires precise operation and high cost.
bionic piezoelectric hair sensor [36]	Piezoelectric function Design based on genetic algorithm	1 Hz-500 Hz	2.21 mV/Pa	Not easy to integrate
AlN diaphragm acoustic transducer [37]	a circular aluminum nitride and silicon nitride unimorph diaphragm and an encapsulated air-filled back cavity	10 Hz-50 kHz-	1.87 µV/Pa	Low sensitivity
Proposed sensor	**Tapered PMF**	**200 Hz-4000 Hz**	**42.4 mV/kPa**	**High sensitivity, simple structure, low cost and easy integration**

4 Conclusion

We designed and demonstrated a high sensitive acoustic sensor based on the MMZI with tapered PMF. Using the optical fiber tapering technology, the PMF was made by gradually changing the MMZI. The transmission spectrum of MMZI will shift with the change of curvature. By attaching the MMZI to the WPD, when an external acoustic pressure worked, it leads to the deformation and vibration of the WPD. The acoustic frequency can be measured in real-time by detecting the vibrating states of the MMZI. The acoustic sensor has a broad frequency response in the range of 200 Hz to 4000 Hz. In the experiments, two sensors were fabricated with different waist diameters of 25.72 μm and 28.39 μm, respectively. The sensitivities of Sensor-1 and Sensor-2 were 42.4 mV/kPa and 29.8 mV/kPa at the frequency of 2000 Hz, respectively. The minimum detectable pressures of Sensor-1 and Sensor-2 were 1.24 Pa/√Hz and 1.26 Pa/√Hz, respectively. The acoustic sensor had the advantages of simple manufacturing, high performance, and low cost, which can be used in fields with high acoustic signal strength requirements, such as monitoring workplace noise in manufacturing, iron and steel, and other industrial applications.

Disclosure statement

No potential conflict of interest was reported by the author(s).

Funding

This work was supported by the National Natural Science Foundation of China [61975075]; Fundamental Research Funds for the Central Universities [021314380095]; Bacis Science Research Project of Nantong [JC2020139, JC2021037]; the Key Lab of Advanced Optical Manufacturing Technologies of Jiangsu Province & Key Lab of Modern Optical Technologies of Education Ministry of China [KJS1858]; Six Talent Peaks Project in Jiangsu Province [KTHY-052].

ORCID

Xiaojun Zhu http://orcid.org/0000-0002-1486-3646

References

[1] F. Poletto, D. Finfer, P. Corubolo, and B. Farina, “Dual wavefields from distributed acoustic sensing measurements,” *Geophysics*, vol. 81, no. 6, pp. D585–D597, Nov. 2016. DOI: 10.1190/geo2016-0073.1.

[2] Y. Wang *et al.*, “A comprehensive study of optical fiber acoustic sensing,” *IEEE Access*, vol. 7, pp. 85821–85837, Jun. 2019. DOI: 10.1109/ACCESS.2019.2924736.

[3] S. Wang *et al.*, "Flexible piezoelectric fibers for acoustic sensing and positioning," *Adv. Electron. Mater*, vol. 3, no. 3, pp. 1600449, Feb. 2017. DOI: 10.1002/aelm.201600449.

[4] Z. Pu, W. Wang, Y. Li, and H. Huang, "Doppler tracking and fast compensation for OFDM transmission via non-stationary underwater platforms," *J. Intell. Fuzzy Syst*, vol. 35, no. 3, pp. 2985–2996, Oct. 2018. DOI: 10.3233/JIFS-169654.

[5] M. Vallee, "The science of listening in bioacoustics research: sensing the animals' sounds," *Theory Cult. Soc*, vol. 35, no. 2, pp. 47–65, Aug. 2017. DOI: 10.1177/0263276417727059.

[6] Y. Y. Weng *et al.*, "A robust and compact fiber Bragg grating vibration sensor for seismic measurement," *IEEE Sens. J*, vol. 12, no. 4, pp. 800–804, Apr. 2012. DOI: 10.1109/JSEN.2011.2166258.

[7] L. Zhao *et al.*, "A fiber strain sensor with high resolution and large measurement scale," *IEEE Sens. J*, vol. 20, no. 6, pp. 2991–2996, Dec. 2019. DOI: 10.1109/JSEN.2019.2958046.

[8] I. Laarossi *et al.*, "Ultrahigh temperature Raman-based distributed optical fiber sensor with gold-coated fiber," *IEEE J. Sel. Top. Quantum Electron*, vol. 23, no. 2, pp. 5601606, Nov. 2016. DOI: 10.1109/JSTQE.2016.2633821.

[9] L. Schenato, A. Galtarossa, A. Pasuto, and L. Palmieri, "Distributed optical fiber pressure sensors," *Opt. Fiber Technol*, vol. 58, pp. 102239, Sept. 2020. DOI: 10.1016/j.yofte.2020.102239.

[10] T. L. Li, Y. G. Tan, P. Xia, and Z. D. Zhou, "Paralleled structure-based string-type fiber Bragg grating acceleration sensor," *IEEE Sens. J*, vol. 17, no. 5, pp. 1325–1332, Mar. 2017. DOI: 10.1109/JSEN.2016.2642145.

[11] H. T. Di, Y. Xin, and J. Q. Jian, "Review of optical fiber sensors for deformation measurement," *Optik*, vol. 168, pp. 703–713, Sept. 2018. DOI: 10.1016/j.ijleo.2018.04.131.

[12] J. A. Bucaro, H. D. Dardy, and E. F. Carome, "Optical fiber acoustic sensor," *Appl. Opt*, vol. 16, no. 7, pp. 1761–1762, Apr. 1977. DOI: 10.1364/AO.16.001761.

[13] M. Pang and W. Jin, "Detection of acoustic pressure with hollow-core photonic bandgap fiber," *Opt. Express*, vol. 17, no. 13, pp. 11088–11097, Jun. 2009. DOI: 10.1364/OE.17.011088.

[14] D. Pawar, C. N. Rao, R. K. Choubey, and S. N. Kale, "Mach-Zehnder interferometric photonic crystal fiber for low acoustic frequency detections," *Appl. Phys. Lett*, vol. 108, no. 4, pp. 041912, Jan. 2016. DOI: 10.1063/1.4940983.

[15] C. L. Lee *et al.*, "Refined bridging of microfiber plugs in hollow core fiber for sensing acoustic vibrations," *IEEE Photonics Technol. Lett*, vol. 27, no. 22, pp. 2403–2406, Nov. 2015. DOI: 10.1109/LPT.2015.2466615.

[16] Y. H. Tseng and J. S. Wang, "Single-crystalline tellurite optical fiber hydrophone," *Opt. Lett*, vol. 41, no. 5, pp. 970–973, Feb. 2016. DOI: 10.1364/OL.41.000970.

[17] T. Fu, P. Wei, X. L. Han, and Q. B. Liu, "Application of fiber Bragg grating acoustic emission sensors in thin polymer-bonded explosives," *Sensors*, vol. 18, no. 11, pp. 3778, Nov. 2018. DOI: 10.3390/s18113778.

[18] J. O. Gaudron, F. Surre, T. Sun, and K. T. V. Grattan, "LPG-based optical fibre sensor for acoustic wave detection," *Sens. Actuator A Phys*, vol. 173, no. 1, pp. 97–101, Jan. 2012. DOI: 10.1016/j.sna.2011.10.023.

[19] X. Fu *et al.*, "Intensity demodulation based fiber sensor for dynamic measurement of acoustic wave and lateral pressure simultaneously," *IEEE Photonics J*, vol. 8, no. 6, pp. 6805713, Dec. 2016. DOI: 10.1109/JPHOT.2016.2627546.

[20] S. L. Woon, K. M. Kwan, W. Y. Chong, H. S. Lin, and C. H. Pua, "Cascaded acoustic wave sensors based on erbium-doped fiber laser dynamics for intrusion zone identification," *IEEE Sens. J*, vol. 17, no. 6, pp. 1893–1898, Mar. 2017. DOI: 10.1109/JSEN.2017.2655019.

[21] J. M. De Freitas, T. A. Birks, and M. Rollings, "Optical micro-knot resonator hydrophone," *Opt. Express*, vol. 23, no. 5, pp. 5850–5860, Mar. 2015. DOI: 10.1364/OE.23.005850.
[22] Q. Z. Rong *et al.*, "Ultrasonic sensitivity-improved Fabry-Perot interferometer using acoustic focusing and its application for noncontact imaging," *IEEE Photonics J*, vol. 9, no. 3, pp. 6802511, May. 2017. DOI: 10.1109/JPHOT.2017.2702719.
[23] J. Wang *et al.*, "Sound source localization based on Michelson fiber optic interferometer array," *Opt. Fiber Technol*, vol. 51, pp. 112–117, May. 2019. DOI: 10.1016/j.yofte.2019.05.008.
[24] S. Qian, H. Chen, Y. Xu, and L. Su, "High sensitivity detection of partial discharge acoustic emission within power transformer by Sagnac fiber optic sensor," *IEEE Trans. Dielectr. Electr. Insul*, vol. 25, no. 6, pp. 2313–2320, Dec. 2018. DOI: 10.1109/TDEI.2018.007131.
[25] C. M. Lan, W. S. Zhou, and Y. W. Xie, "Detection of ultrasonic stress waves in structures using 3D shaped optic fiber based on a Mach-Zehnder interferometer," *Sensors*, vol. 18, no. 4, pp. 1218, Apr. 2018. DOI: 10.3390/s18041218.
[26] W. H. Zhu, D. Y. Li, J. J. Liu, and R. H. Wang, "Membrane-free acoustic sensing based on an optical fiber Mach-Zehnder interferometer," *Appl. Opt*, vol. 59, no. 6, pp. 1775–1779, Feb. 2020. DOI: 10.1364/AO.381002.
[27] S. Dass and R. Jha, "Micro-tip cantilever as low frequency microphone," *Sci. Rep*, vol. 8, no. 1, pp. 12701, Aug. 2018. DOI: 10.1038/s41598-018-31062-9.
[28] Y. Zhao, F. Xia, M. Q. Chen, and R. Q. Lv, "Optical fiber low-frequency vibration sensor based on Butterfly-shape Mach-Zehnder interferometer," *Sens. Actuator A Phys*, vol. 273, pp. 107–112, Apr. 2018. DOI: 10.1016/j.sna.2018.01.051.
[29] Y. Jung, G. Brambilla, and D. J. Richardson, "Broadband single-mode operation of standard optical fibers by using a sub-wavelength optical wire filter," *Opt Express*, vol. 16, no. 19, pp. 14661–14667, Sept. 2008. DOI: 10.1364/OE.16.014661.
[30] W. D. Qu and H. L. Tang, *Mechanical Vibration Manual*. Beijing, China: machinery Industry Press, 2000.
[31] O. Tabata, K. Kawahata, S. Sugiyama, and I. Igarashi, "Mechanical property measurements of thin films using load-deflection of composite rectangular membranes," *Sens. Actuators*, vol. 20, no. 1–2, pp. 135–141, Nov. 1989. DOI: 10.1016/0250-6874(89)87111-2.
[32] M. D. Giovanni, *Flat and Corrugated Diaphragm Design Handbook*. Boca Raton, FL, Marcel Dekker,1982.
[33] S. N. Wu, L. Wang, X. L. Chen, and B. Zhou, "Flexible optical fiber Fabry-Perot interferometer based acoustic and mechanical vibration sensor," *J. Lightwave Technol*, vol. 36, no. 11, pp. 2216–2221, Feb. 2018. DOI: 10.1109/JLT.2018.2810090.
[34] S. Dass and R. Jha, "Tapered fiber attached nitrile diaphragm-based acoustic sensor," *J. Lightwave Technol*, vol. 35, no. 24, pp. 5411–5417, Nov. 2017. DOI: 10.1109/JLT.2017.2776519.
[35] C. Luo *et al.*, "All-fiber sensor based on few-mode fiber offset splicing structure cascaded with long-period fiber grating for curvature and acoustic measurement," *Photonic Netw. Commun*, vol. 32, no. 2, pp. 224–229, Feb. 2016. DOI: 10.1007/s11107-016-0604-9.
[36] Y. Wang, J. Zhao, Y. Xia, and P. B. Liu, "Configuration optimization of bionic piezoelectric hair sensor for Acoustic/Tactile detection," *Bioinspir. Biomim*, vol. 15, no. 5, pp. 056015, Sept. 2020. DOI: 10.1088/1748-3190/ab8f6c.
[37] A. E. Hake, C. M. Zhao, L. C. Ping, and K. Grosh, "Ultraminiature AlN diaphragm acoustic transducer," *Appl. Phys. Lett*, vol. 117, no. 14, pp. 143504, Oct. 2020. DOI: 10.1063/5.0020645.